Virtual-Admittance Parameter Impact on Damping Provision from Grid-Forming Controlled Converters

Virtual-Admittance Parameter Impact on Damping Provision from Grid-Forming Controlled Converters

Anant Narula, Paul Imgart, and Mebtu Beza
Chalmers University of Technology
Göteborg, Sweden
anant.narula@chalmers.se

Jan R. Svensson
Hitachi Energy Research
Västerås
Sweden

Jean-Philippe Hasler
Hitachi Energy
Västerås
Sweden

***Abstract*—Grid-forming (GFM) converter control is a control approach to address several of the challenges associated with increased proliferation of power-electronic converters in electrical power grids. Virtual-admittance (VA) based GFM control structures allow to shape the converter's frequency response, and control structures like the decoupled GFM controller enable the independent tuning of virtual resistance and virtual inductance. This raises the need for effective tuning methods covering the different aspects of converter performance that are influenced by the choice of VA parameters. This paper presents a simplified method to study the impact of VA parameters on the provision of passive damping from a GFM-controlled converter and compares it to a power-response matrix-based analysis. The findings are verified using time-domain simulations.**

I. Introduction

In response to decarbonization goals, electric power grids see a growing share of power-electronic converters in generation and transmission. Various challenges associated with this transition, such as reduced system inertia and lower short-circuit levels, are addressed by the concept of grid-forming (GFM) converter control, which implies controlling the converter to act as a slowly varying voltage source behind an impedance [1], [2], [3].

Among the variety of GFM control approaches, the virtual-admittance (VA) based approach stands out due to the possibility to shape the converter's behaviour in the frequency domain by tuning the VA [4], [5], [6]. Recent improvements of this GFM control approach, e.g. the decoupled GFM control, allow for the independent choice of VA parameters without introducing undesirable power coupling. This new design freedom comes with the need to identify effective tuning methods for these control parameters [7], [8].

The existing tuning methods for VA parameters typically focus on aspects such as stability studies [9], [10], [11], steady-state reactive power sharing [12], [13], [14], or current limitation [15], [16]. However, the decoupled GFM controller makes it possible and necessary to tune the VA parameters based on their impact on the converter's behaviour over a wide frequency range, considering the impact of these parameters even within the stable design region. Furthermore, the previous limitation to high X/R ratios due to the negative effects introduced by power coupling is addressed by the decoupling mechanism of the decoupled controller, enabling free and independent selection of both parameters [7], [17].

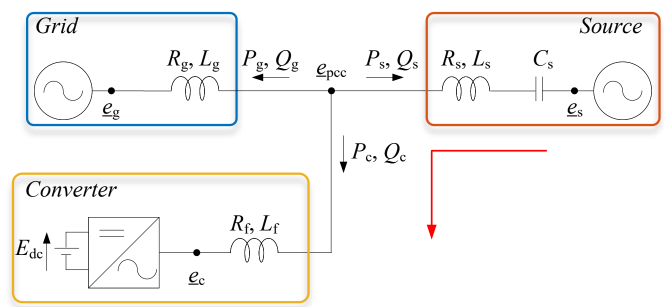

Fig. 1: Single line diagram of the investigated system model.

VA parameters have an impact on many aspects of GFM controlled converter performance, such as contribution to grid strength and short-circuit current, harmonic behaviour, as well as on converter system design aspects like energy-storage sizing. This means that the tuning of these parameters requires careful application-specific prioritisation of these different, often conflicting goals.

This paper demonstrates a simple and effective method to study the impact of the VA parameters of a GFM-controlled converter on the provision of passive damping, i.e. damping provided without the addition of explicit damping controllers. To achieve this, the converter's impact on the resonance is at first studied by representing the converter through its VA instead of the full input admittance. This approach is then verified with the help of power-response matrix (PRM) based models using the full input-admittance representation [18], and validated using detailed time-domain simulations.

II. System Model and Controller Description

The system model and control strategy described in this section have been chosen to demonstrate the impedance-based method of studying the VA parameters' impact on damping provision from a GFM controlled converter. The method is valid even in other system configurations.

A. *Investigated System Model*

The investigated system model is shown in Fig. 1 and consists of two fixed voltage sources, representing the grid and a connected generator, with a voltage-source (VSC) converter connected in shunt to their interconnection. The connection of the generator to the grid also contains a capacitor, giving rise to a resonance. This model is a simplified representation of e.g. a group of generators connected to a distanced grid with a series compensated line, or an offshore wind power plant connected to the onshore grid by a submarine ac cable. To be able to demonstrate the impact of the converter's VA parameters on the resonance more clearly, the converter is electrically closer to the source of the resonance: $L_\mathrm{s} < L_\mathrm{g}$.

B. Decoupled GFM Control

The proposed study method requires that the converter's input admittance can be assumed to be equal to the VA in the frequency region of interest. This is the case for the decoupled GFM control introduced in [7], a GFM controller which allows to freely select both the resistive and inductive part of the VA without causing power coupling. Using this control, the converter's input admittance in the converter's synchronous reference frame is given as

$$\mathbf{Y}_\mathrm{conv} = \mathbf{Y}_\mathrm{v}\frac{s^2}{(s+\alpha)^2} \quad \text{with } \mathbf{Y}_\mathrm{v} = (R_\mathrm{v} + sL_\mathrm{v} + \mathrm{j}\omega_\mathrm{b}L_\mathrm{v})^{-1}, \tag{1}$$

where α is the closed-loop bandwidth of the active- and reactive-power controllers (here assumed to be the same), R_v and L_v are the virtual resistance and inductance, respectively, ω_b is the rated angular frequency, the active- and reactive-power references are assumed to be 0, and the virtual-reactor dynamics are included [7].

III. Proposed Method to Study Virtual Admittance Parameter Damping Impact

As can be seen from (1), the converter input admittance as seen from the PCC can be approximated by its VA for the frequency regions outside the bandwidth of the outer control loops, i.e., in the sub-synchronous and super-synchronous ranges sufficiently far from the nominal grid frequency in the stationary reference frame[1]. This approximation enabled by the decoupled GFM control structure allows a direct interpretation of the VA parameters' influence on the damping contribution of the converter in these frequency regions.

To influence the damping of an existing grid resonance, the converter must actively participate in the resonant mode. In other words, it must (i) provide a sufficiently low-impedance path for the resonant current, and (ii) dissipate part of the oscillatory energy associated with the resonance. While lower values of virtual resistance and inductance increase resonance participation by reducing the impedance magnitude, a higher virtual resistance enhances energy dissipation. This trade-off can be demonstrated formally using the following relations.

[1]Refer to Fig. 2 for an illustration of the power controllers' impact in both stationary and synchronous reference frame

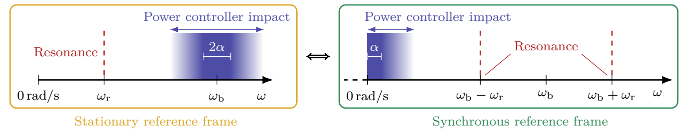

Fig. 2: Illustration of the frequency shift due to change of reference frame depicting a resonance frequency and the frequency region where the power controllers determine the converter's behaviour.

Consider the series RLC path indicated by the red arrow in Fig. 1. The maximum stored energy in the inductive elements in this path at resonance is given by

$$W_\mathrm{max} = (L_\mathrm{v} + L_\mathrm{s})I_\mathrm{v}^2 \approx L_\mathrm{v}I_\mathrm{v}^2 \quad \because L_\mathrm{s} << L_\mathrm{v}, \tag{2}$$

and the energy dissipated per cycle is

$$W_\mathrm{diss} = I_\mathrm{v}^2(R_\mathrm{v} + R_\mathrm{s})\frac{2\pi}{\omega_r} \approx I_\mathrm{v}^2 R_\mathrm{v}\frac{2\pi}{\omega_r} \quad \because R_\mathrm{s} << R_\mathrm{v}, \tag{3}$$

where I_v denotes the RMS value of the resonant current flowing into the converter (and consequently through the virtual impedance) and ω_r is the angular resonance frequency. The corresponding homogeneous equation of the series RLC path is given by

$$\frac{d^2 i_\mathrm{v}}{dt^2} + \frac{(R_\mathrm{v} + R_\mathrm{s})}{(L_\mathrm{v} + L_\mathrm{s})}\frac{di_\mathrm{v}}{dt} + \frac{1}{(L_\mathrm{v} + L_\mathrm{s})C_\mathrm{s}}i_\mathrm{v} = 0, \tag{4}$$

with i_v denoting the instantaneous value of the resonant current. By comparing (4) with the standard second-order form given by

$$\frac{d^2 x}{dt^2} + 2\zeta_\mathrm{r}\omega_\mathrm{r}\frac{dx}{dt} + \omega_\mathrm{r}^2 x = 0, \tag{5}$$

and utilizing (2) and (3), the damping ratio ζ_r of the resonant mode with natural angular frequency ω_r can be expressed in energy form as

$$\zeta_\mathrm{r} = \frac{W_\mathrm{diss}}{4\pi W_\mathrm{max}}. \tag{6}$$

Assuming that a change in the virtual impedance parameters only has a negligible impact on the PCC voltage, the impedance relation of the virtual branch,

$$I_\mathrm{v} \propto \frac{1}{|\underline{Z}_\mathrm{v}|}, \quad \text{with } \underline{Z}_\mathrm{v} = R_\mathrm{v} + j\omega_\mathrm{r}L_\mathrm{v}, \tag{7}$$

can be utilized together with (2) and (3) to obtain the following proportionality relations for a constant ratio $R_\mathrm{v}/L_\mathrm{v}$:

$$I_\mathrm{v} \propto \frac{1}{L_\mathrm{v}}, \qquad W_\mathrm{max} \propto \frac{1}{L_\mathrm{v}}, \qquad W_\mathrm{diss} \propto \frac{1}{L_\mathrm{v}}. \tag{8}$$

From (8) follows that increasing L_v reduces I_v, therefore decreasing the participation of the converter in the resonant mode. Furthermore, since both W_max and W_diss are inversely proportional to L_v, from (6) it follows that varying L_v while maintaining a constant $R_\mathrm{v}/L_\mathrm{v}$ ratio has a negligible effect on the damping ratio ζ_r.

The influence of R_v can be examined using

$$I_\mathrm{v}^2 \propto \frac{1}{R_\mathrm{v}^2 + (\omega_\mathrm{r}L_\mathrm{v})^2}. \tag{9}$$

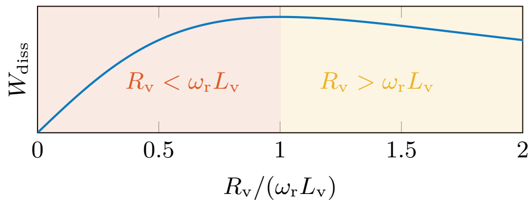

Fig. 3: Qualitative illustration of the impact of R_{v} on W_{diss} for $\omega_{\mathrm{r}} = 0.4\,\mathrm{pu}$, as given by (10).

For $R_{\mathrm{v}} < \omega_{\mathrm{r}} L_{\mathrm{v}}$ and constant L_{v}, (9) indicates that variations in R_{v} have a comparatively smaller influence on I_{v} than variations in L_{v}. Still, increasing R_{v} in this region decreases I_{v} and correspondingly W_{max} decreases according to (2). However, in this operating region, increasing R_{v} increases W_{diss}. This can be understood by substituting (9) in (3) using a proportionality constant k, which results in

$$W_{\mathrm{diss}} \approx \frac{k}{R_{\mathrm{v}}^2 + (\omega_{\mathrm{r}} L_{\mathrm{v}})^2} R_{\mathrm{v}} \frac{2\pi}{\omega_r}. \tag{10}$$

Using (10), the impact of variations in R_{v} on W_{diss} is illustrated in Fig. 3. It can be observed from the figure that in the region where $R_{\mathrm{v}} < \omega_{\mathrm{r}} L_{\mathrm{v}}$, an increase in the value of R_{v} increases W_{diss}. An increase in W_{diss} together with a decrease in W_{max} imply an increasing ζ_{r} according to (6). Thus, in this operating region, raising R_{v} effectively enhances damping without significantly reducing resonance participation.

Conversely, for $R_{\mathrm{v}} > \omega_{\mathrm{r}} L_{\mathrm{v}}$ and constant L_{v}, increasing R_{v} significantly reduces I_{v}, thereby limiting the participation of the converter in the resonant mode. In this region, the energy dissipated per cycle also decreases with increasing R_{v}, as illustrated in Fig. 3, due to the strong reduction in current magnitude. Consequently, the capability of the converter to influence the damping of the prevailing grid resonance is diminished.

In summary, within the frequency range outside the bandwidth of the outer control loops, a small L_{v} promotes converter participation in the resonant mode. Moreover, selecting $R_{\mathrm{v}} = \omega_{\mathrm{r}} L_{\mathrm{v}}$ yields an optimal trade-off between resonance participation and energy dissipation, resulting in maximum damping of the resonant mode. The decoupled GFM control provides the flexibility to independently tune the virtual resistance and virtual inductance, thereby enabling systematic selection of VA parameters for effective damping of grid resonances.

IV. Converter Location Impact

In this section, the impact of converter's location on its ability to passively provide damping to the existing grid resonance outside the bandwidth of outer control loops is investigated. Figure 4 shows the equivalent circuit representation of the investigated system model (see Fig. 1) for the resonance analysis of interest. Using the circuit equations, the resonant current flowing into the converter, $\underline{I}_{\mathrm{v}}$, is given by

$$\underline{I}_{\mathrm{v}} = \frac{\underline{E}_{\mathrm{s}}}{\underline{Z}_{\mathrm{s}} + \underline{Z}_{\mathrm{v}}(1 + \underline{Z}_{\mathrm{s}} \underline{Z}_{\mathrm{g}}^{-1})}. \tag{11}$$

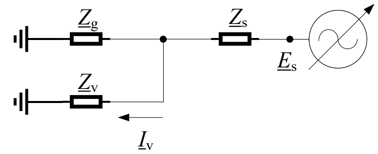

Fig. 4: Equivalent circuit representation of the investigated system model for resonance analysis.

From (11) can be inferred that for a given virtual impedance, the resonant converter current magnitude increases with a decrease in the impedance of the source or with an increase of the grid impedance. In other words, the closer the converter is to the source, the more it participates in the resonance mode, and hence the greater is its ability to dampen it.

V. Small-Signal Analysis

To verify the proposed method to study the VA parameters' impact, the small-signal behaviour of the system configuration shown in Fig. 1 is analysed using PRM-based models [18].

A. Power-Response Matrix-Based Modeling

For the small-signal analysis, the overall system is decomposed into three distinct subsystems: the grid, the source, and the converter, as illustrated with different colors in Fig. 1.

Each subsystem is represented by its corresponding PRM. For instance, the converter subsystem is modeled by considering variations in the PCC voltage as inputs, while the resulting power variations at the converter subsystem terminals are treated as outputs. This relationship is expressed as

$$\begin{bmatrix} \Delta P_{\mathrm{c}} \\ \Delta Q_{\mathrm{c}} \end{bmatrix} = \mathbf{G}_{\mathrm{c}} \begin{bmatrix} \Delta E_{\mathrm{pcc}} \\ \Delta \omega_{\mathrm{pcc}} \end{bmatrix}, \tag{12}$$

where "Δ" denotes small-signal perturbations around the steady-state operating point and $\mathbf{G}_{\mathrm{c}}$ is the converter's PRM.

Similarly, the small-signal models of the grid and source subsystems are given by

$$\begin{bmatrix} \Delta P_{\mathrm{g}} \\ \Delta Q_{\mathrm{g}} \end{bmatrix} = \mathbf{G}_{\mathrm{g}} \begin{bmatrix} \Delta E_{\mathrm{pcc}} \\ \Delta \omega_{\mathrm{pcc}} \end{bmatrix}, \tag{13}$$

$$\begin{bmatrix} \Delta P_{\mathrm{s}} \\ \Delta Q_{\mathrm{s}} \end{bmatrix} = \mathbf{G}_{\mathrm{s}} \begin{bmatrix} \Delta E_{\mathrm{pcc}} \\ \Delta \omega_{\mathrm{pcc}} \end{bmatrix} + \mathbf{G}'_{\mathrm{s}} \begin{bmatrix} \Delta E_{\mathrm{s}} \\ \Delta \omega_{\mathrm{s}} \end{bmatrix}, \tag{14}$$

respectively. It should be noted that the PRM for each subsystem is defined according to the convention that power flowing into the respective subsystem is positive. A comprehensive analytical derivation of these transfer matrices will be provided in the final version of the manuscript and is omitted here due to space constraints.

Once the PRMs of the individual subsystems are obtained, the overall closed-loop response of the system can be derived by applying Kirchhoff's laws and performing appropriate algebraic substitutions. For example, the power variations at the terminals of each subsystem resulting from disturbances in the source voltage can be expressed as

$$\begin{bmatrix} \Delta P_{\mathrm{g}} & \Delta Q_{\mathrm{g}} & \Delta P_{\mathrm{s}} & \Delta Q_{\mathrm{s}} & \Delta P_{\mathrm{c}} & \Delta Q_{\mathrm{c}} \end{bmatrix}^{\mathrm{T}} = \mathbf{G} \begin{bmatrix} \Delta E_{\mathrm{s}} \\ \Delta \omega_{\mathrm{s}} \end{bmatrix}. \tag{15}$$

TABLE I: System and control parameters for the case studies.

S_b	480 MVA (1 pu)	V_b	220 kV (1 pu)
L_g	0.5 pu	R_g	0.05 pu
L_s	0.167 pu	R_s	0.0167 pu
C_s	5.0 pu	S_c	112 MVA
L_f	0.643 pu	R_f	0.0643 pu
L_v	1.0714 pu	R_v	0.268 pu
ω_b	314.16 rad/s	α	2π 1 rad/s

By examining the Bode plots of the elements of the transfer matrix $\mathbf{G}$, the small-signal behavior of the system can be systematically analyzed. This facilitates the evaluation of damping characteristics and resonance frequencies of the system modes, as well as the investigation of potential dynamic interactions among the subsystems. The following subsection illustrates this analysis through representative case studies.

B. Case Studies

Unless otherwise stated, the system and control parameters listed in Table I are used to generate the Bode plots presented in this subsection. The operating point is defined such that the converter injects zero active and reactive power at the PCC in steady state. The grid and source voltages are set to $1\,\mathrm{pu}\angle 5°$ and $1\,\mathrm{pu}\angle 0°$, respectively.

1) Influence of Varying Virtual Inductance: First, the influence of varying the virtual inductance while maintaining a constant ratio $R_\mathrm{v}/L_\mathrm{v}$ is investigated. The analysis focuses on the reactive power responses of the grid, source, and converter subsystems to variations in the source voltage magnitude, ΔE_s. These correspond to the transfer function elements $\mathbf{G}_{2,1}$, $\mathbf{G}_{4,1}$, and $\mathbf{G}_{6,1}$ in (15), respectively.

Figure 5 presents the frequency responses of $\mathbf{G}_{2,1}$, $\mathbf{G}_{4,1}$, and $\mathbf{G}_{6,1}$, shown in blue, red, and yellow, respectively, for $L_\mathrm{v} = 1.0714\,\mathrm{pu}$ (solid curves) and $L_\mathrm{v} = 2.143\,\mathrm{pu}$ (dashed curves). The yellow magnitude response reduces at the resonance as L_v is increased, meaning the participation of the converter subsystem in the resonance decreases. This is reflected by the difference between the magnitude responses of the source and the grid decreasing as L_v increases while the phase responses remain opposite, which indicates a stronger interaction between these two subsystems. Moreover, Fig. 5 shows that the slope of the magnitude responses around the resonant modes remains nearly unchanged for the two values of virtual inductance, indicating a similar damping ratio in both cases.

2) Influence of Varying Virtual Resistance: Next, the influence of varying the virtual resistance is examined while keeping $L_\mathrm{v} = 1.0714\,\mathrm{pu}$ constant. Figure 6 shows the frequency responses of $\mathbf{G}_{2,1}$, $\mathbf{G}_{4,1}$, and $\mathbf{G}_{6,1}$ for $R_\mathrm{v} = 0.268\,\mathrm{pu}$ (solid curves) and $R_\mathrm{v} = 0.643\,\mathrm{pu}$ (dashed curves).

At the resonant modes, the difference between the magnitude responses of the source and grid subsystems decreases as the virtual resistance increases, indicating reduced participation of the converter subsystem in the resonance, similar to the previous case. In contrast to the virtual inductance variation, however, the slope of the magnitude responses around the resonant modes decreases with increasing virtual resistance. This implies that the damping ratio of the resonant mode increases for higher values of virtual resistance.

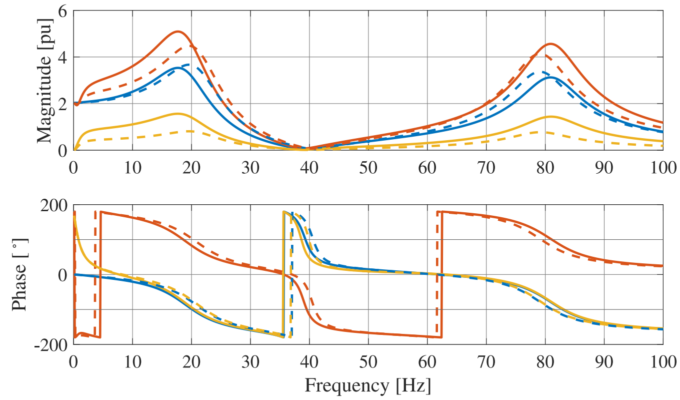

Fig. 5: Frequency response of closed-loop transfer functions from source voltage magnitude variations to reactive power variations in the grid subsystem (blue), source subsystem (red), and converter subsystem (yellow) for $L_\mathrm{v} = 1.0714\,\mathrm{pu}$ (solid curves) and $L_\mathrm{v} = 2.143\,\mathrm{pu}$ (dashed curves).

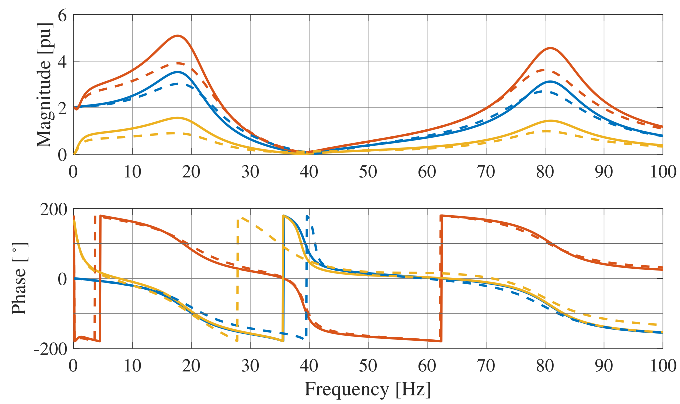

Fig. 6: Frequency response of closed-loop transfer functions from source voltage magnitude variations to reactive power variations in the grid subsystem (blue), source subsystem (red), and converter subsystem (yellow) for $R_\mathrm{v} = 0.268\,\mathrm{pu}$ (solid curves) and $R_\mathrm{v} = 0.643\,\mathrm{pu}$ (dashed curves).

Furthermore, the case where $R_\mathrm{v} > \omega_\mathrm{r} L_\mathrm{v}$ is investigated. Figure 7 presents the corresponding frequency responses for $R_\mathrm{v} = 0.643\,\mathrm{pu}$ (dashed curves) and $R_\mathrm{v} = 1.0714\,\mathrm{pu}$ (dotted curves). At the resonant modes, the difference between the magnitude responses of the source and grid subsystems decreases further as the virtual resistance increases, indicating an additional reduction in the participation of the converter subsystem in the resonance. However, the slope of the magnitude responses around the resonant modes remains nearly unchanged when R_v exceeds $\omega_\mathrm{r} L_\mathrm{v}$. This suggests that further increasing the virtual resistance beyond this threshold does not significantly affect the damping ratio of the resonant mode.

3) Influence of Varying Converter Location: Finally, the influence of the converter location is investigated by moving the converter closer to the grid subsystem. Accordingly, the

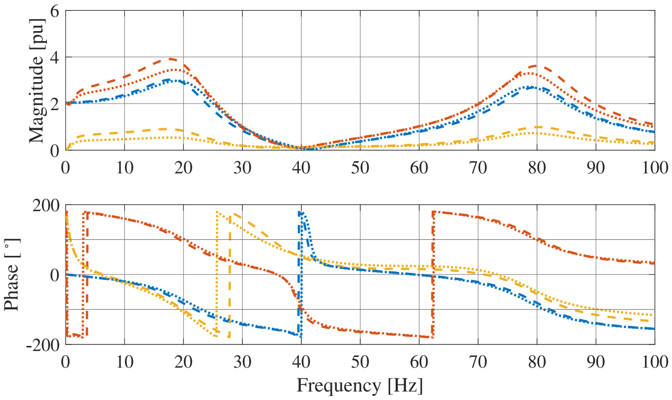

Fig. 7: Frequency response of closed-loop transfer functions from source voltage magnitude variations to reactive power variations in the grid subsystem (blue), source subsystem (red), and converter subsystem (yellow) for $R_{\mathrm{v}} = 0.643\,\mathrm{pu}$ (dashed curves) and $R_{\mathrm{v}} = 1.0714\,\mathrm{pu}$ (dotted curves).

grid and source impedances are selected as $L_{\mathrm{g}} = 0.167$ pu, $R_{\mathrm{g}} = 0.0167$ pu, and $L_{\mathrm{s}} = 0.5$ pu, $R_{\mathrm{s}} = 0.05$ pu, respectively. Figure 8 presents the frequency responses of $\mathbf{G}_{2,1}$, $\mathbf{G}_{4,1}$, and $\mathbf{G}_{6,1}$ for $R_{\mathrm{v}} = 0.268\,\mathrm{pu}$ (solid curves) and $R_{\mathrm{v}} = 0.643\,\mathrm{pu}$ (dashed curves). It can be observed that the participation of the converter subsystem in the resonant modes is minimal. Consequently, even in the operating region where $R_{\mathrm{v}} < \omega_{\mathrm{r}} L_{\mathrm{v}}$, increasing the virtual resistance does not significantly improve the damping ratio of the resonant mode.

In summary, the small-signal analysis presented in this section confirms the validity of the proposed method to study the VA parameters' impact. The observed trends in modal interaction, resonance characteristics, and damping behaviour under variations of the VA parameters are consistent with the analytical insights derived in the previous section. Therefore, the frequency-domain results obtained from the PRM-based modelling framework further substantiate the theoretical analysis.

VI. Simulation Verification

To further validate the impact analysis of the VA parameters, detailed time-domain simulations of the system configuration shown in Fig. 1 are conducted in PSCAD. Unless otherwise stated, the system and control parameters listed in Table 1 are used for all simulation case studies.

A step decrease of $0.05\,\mathrm{pu}$ is applied to the magnitude of the source voltage at $0.1\,\mathrm{s}$ in order to trigger the system's resonances, which are observable in both active and reactive power. Figure 9 depicts the active power response of the source subsystem following the applied disturbance. Consistent with the analytical findings presented in the previous section, the figure shows that power oscillations at approximately $20\,\mathrm{Hz}$ and $80\,\mathrm{Hz}$ are excited by the disturbance. Furthermore, the damping of these two oscillatory modes remains unchanged for the two different values of the virtual inductance, i.e., $L_{\mathrm{v}} = 1.0714\,\mathrm{pu}$ and $L_{\mathrm{v}} = 2.143\,\mathrm{pu}$.

To examine the influence of the virtual resistance, the same disturbance is applied and the resulting power variations in the

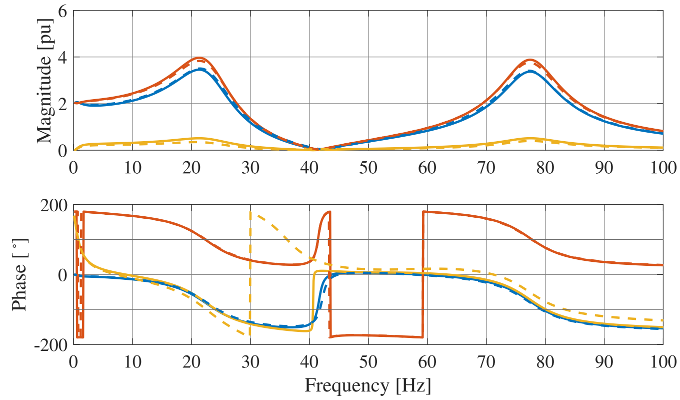

Fig. 8: Frequency responses of the closed-loop transfer functions from source-voltage magnitude variations to reactive-power variations in the grid subsystem (blue), source subsystem (red), and converter subsystem (yellow) for $R_{\mathrm{v}} = 0.268\,\mathrm{pu}$ (dashed curves) and $R_{\mathrm{v}} = 0.643\,\mathrm{pu}$ (dotted curves), in the case where the converter is located closer to the grid subsystem.

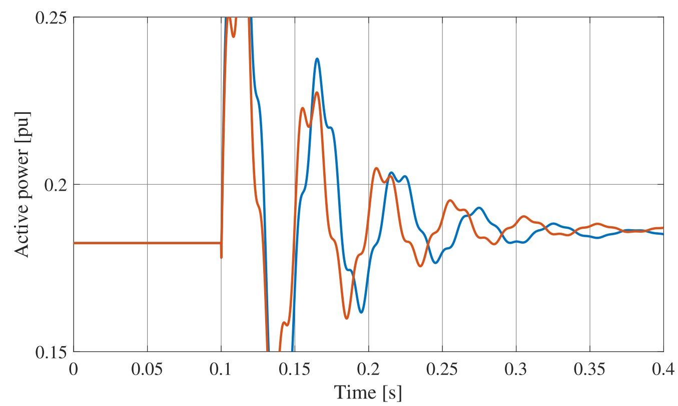

Fig. 9: Time-domain response of the active power variations in the source subsystem due to the applied disturbance in the magnitude of the source voltage for $L_{\mathrm{v}} = 1.0714$ p.u. (blue curve) and $L_{\mathrm{v}} = 2.143$ p.u. (red curve).

source subsystem are analyzed. As shown in Fig. 10, increasing R_{v} from $0.268\,\mathrm{pu}$ to $0.643\,\mathrm{pu}$ significantly improves the damping of the resonant modes. However, when the virtual resistance is further increased from $0.643\,\mathrm{pu}$ to $1.0714\,\mathrm{pu}$, no noticeable improvement in the damping of the two modes is observed.

Finally, to investigate the influence of the converter location, the grid and source impedances are adjusted according to the values specified in the previous section. The same disturbance is then applied, and the resulting power variations in the source subsystem are analyzed. As shown in Fig. 11, increasing R_{v} from $0.268\,\mathrm{pu}$ to $0.643\,\mathrm{pu}$ does not result in a noticeable improvement in the damping of the two modes.

Overall, the simulation results presented in this section validate the analytical findings discussed in the previous section.

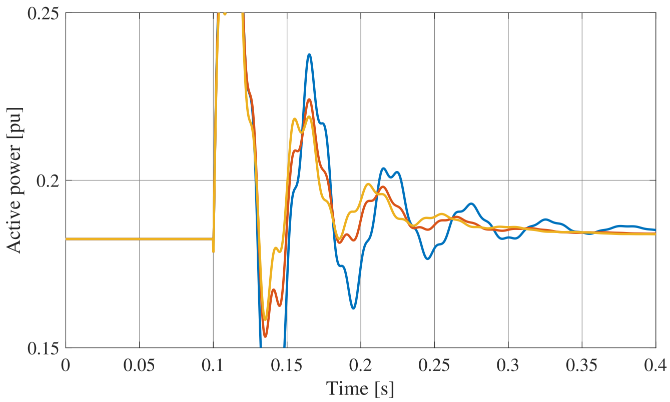

Fig. 10: Time-domain response of the active power variations in the source subsystem due to the applied disturbance in the magnitude of the source voltage for $R_\mathrm{v} = 0.268$ p.u. (blue curve), $R_\mathrm{v} = 0.643$ p.u. (red curve), and $R_\mathrm{v} = 1.0714$ p.u. (yellow curve).

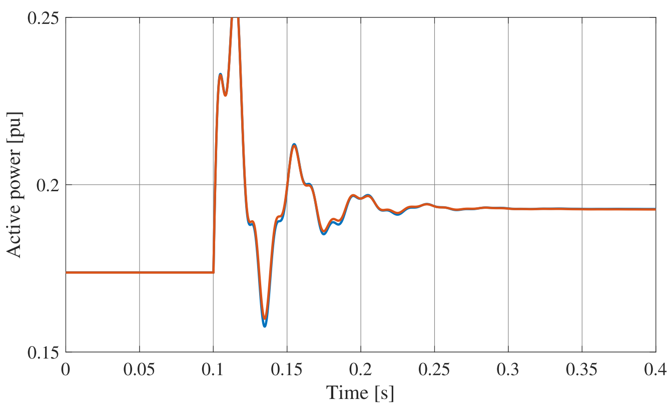

Fig. 11: Time-domain response of the active power variations in the source subsystem due to the applied disturbance in the source-voltage magnitude for $R_\mathrm{v} = 0.268\,\mathrm{pu}$ (blue curve) and $R_\mathrm{v} = 0.643\,\mathrm{pu}$ (red curve), in the case where the converter is located closer to the grid subsystem.

VII. Conclusion

This paper has shown that PRM-based modelling can be effectively used to identify the impact of VA parameters on the provision of passive damping by a GFM-controlled converter. The results further show that, for the decoupled GFM control, the converter behaviour in the higher subsynchronous frequency range can be accurately represented by its VA, allowing to represent the converter by its VA to study the VA parameters damping impact. Finally, the analysis of the studied system shows that a decrease in the virtual inductance increases the participation of the shunt-connected converter in resonance within a series-compensated transmission network, while causing no significant change in the damping ratio of the resonance. Increasing the virtual resistance up to the value of the virtual reactance at the resonance frequency primarily enhances the damping of the resonance. However, further increases in the virtual resistance do not lead to additional improvements in damping.

References

[1] J. Matevosyan et al., "Grid-Forming Inverters: Are They the Key for High Renewable Penetration?" *IEEE Power and Energy Magazine*, vol. 17, no. 6, pp. 89–98, Nov. 2019.

[2] C. Cardozo et al., "Promises and Challenges of Grid Forming: Transmission System Operator, Manufacturer and Academic View Points," *Electric Power Systems Research*, vol. 235, p. 110 855, Oct. 1, 2024.

[3] Y. Lamrani et al., "On the stabilizing contribution of different grid-forming controls to power systems," *IET Generation, Transmission & Distribution*, vol. 18, no. 23, 2024.

[4] P. Rodriguez et al., "Control of grid-connected power converters based on a virtual admittance control loop," in *2013 15th European Conference on Power Electronics and Applications (EPE)*, Sep. 2013, pp. 1–10.

[5] R. Rosso et al., "Grid-Forming Converters: Control Approaches, Grid-Synchronization, and Future Trends — A Review," *IEEE Open Journal of Industry Applications*, vol. 2, pp. 93–109, 2021.

[6] A. Narula et al., "Comparison of Grid-Forming Converter Control Strategies," in *2021 IEEE Energy Conversion Congress and Exposition (ECCE)*, Oct. 2021, pp. 361–368.

[7] P. Imgart et al., "Decoupled PQ Grid-Forming Control With Tunable Converter Frequency Behavior," *IEEE Open Journal of Industry Applications*, vol. 7, pp. 148–162, 2026.

[8] P. Imgart, "Beyond Virtual Synchronous Machine Control," Chalmers University of Technology, 2025.

[9] J. He and Y. W. Li, "Analysis, Design, and Implementation of Virtual Impedance for Power Electronics Interfaced Distributed Generation," *IEEE Transactions on Industry Applications*, vol. 47, no. 6, pp. 2525–2538, Nov. 2011.

[10] A. Bolzoni et al., "Impact of Line and Control Parameters on Droop Stability in Inverters for Distributed Generation," *IEEE Transactions on Smart Grid*, vol. 9, no. 6, Nov. 2018.

[11] W. Zhang et al., "Parameters Tuning of Flexible Drooped Synchronous Power Controller Based on Small Signal Modeling and Sensitivity Analysis," in *2023 IEEE 18th Conference on Industrial Electronics and Applications (ICIEA)*, Aug. 2023.

[12] J. He et al., "An Islanding Microgrid Power Sharing Approach Using Enhanced Virtual Impedance Control Scheme," *IEEE Transactions on Power Electronics*, vol. 28, no. 11, Nov. 2013.

[13] R. An et al., "Successive-Approximation-Based Virtual Impedance Tuning Method for Accurate Reactive Power Sharing in Islanded Microgrids," *IEEE Transactions on Power Electronics*, vol. 36, no. 1, pp. 87–102, Jan. 2021.

[14] J. Zhang et al., "Adaptive Virtual Impedance Control Strategy for Multiple Grid-forming Converters in Islanded Microgrid," in *2023 2nd Asia Power and Electrical Technology Conference (APET)*, Dec. 2023.

[15] A. D. Paquette and D. M. Divan, "Virtual Impedance Current Limiting for Inverters in Microgrids With Synchronous Generators," *IEEE Transactions on Industry Applications*, vol. 51, no. 2, pp. 1630–1638, Mar. 2015.

[16] T. Qoria et al., "Critical Clearing Time Determination and Enhancement of Grid-Forming Converters Embedding Virtual Impedance as Current Limitation Algorithm," *IEEE Journal of Emerging and Selected Topics in Power Electronics*, vol. 8, no. 2, pp. 1050–1061, Jun. 2020.

[17] Z. Tang et al., "A Review of Coupling and Interaction Studies of Grid-Forming Converters Based on Transient Stability," in *2024 7th International Conference on Energy, Electrical and Power Engineering (CEEPE)*, Apr. 2024, pp. 259–265.

[18] A. Narula et al., "Power-Response Matrix-Based Modeling of Converter Systems for Small-Signal Analysis," in *2024 IEEE Energy Conversion Congress and Exposition (ECCE)*, Phoenix, AZ, USA: IEEE, Oct. 20, 2024, pp. 4724–4731.